50th AIAA Aerospace Sciences Meeting including the New Horizons Forum and Aerospace Exposition
09 - 12 January 2012, Nashville, Tennessee

AIAA 2012-0423

Extensions of Time Spectral Methods for Practical Rotorcraft Problems

Dimitri J. Mavriplis * Zhi Yang † Nathan Mundis ‡

Department of Mechanical Engineering, University of Wyoming, Laramie, WY 82071

For flows with strong periodic content, time-spectral methods can be used to obtain time-accurate solutions at substantially reduced cost compared to traditional time-implicit methods which operate directly in the time domain. In their original form, time spectral methods are applicable only to purely periodic problems and formulated for single grid systems. A wide class of problems involve quasi-periodic flows, such as maneuvering rotorcraft problems, where a slow transient is superimposed over a more rapid periodic motion. Additionally, the most common approach for simulating combined rotor-fuselage interactions is through the use of a dynamically overlapping mesh system. Thus, in order to represent a practical approach for rotorcraft simulations, time spectral methods that are applicable to quasi-periodic problems and capable of operating on overlapping mesh systems need to be formulated. In this paper, we propose separately an extension of time spectral methods to quasi-periodic problems, and an extension for overlapping mesh configurations. In both cases, the basic implementation allows for two levels of parallelism, one in the spatial dimension, and another in the time-spectral dimension, and is implemented in a modular fashion that minimizes the modifications required to an existing steady-state solver. Results are given for three-dimensional quasi-periodic problems on a single mesh, and for two-dimensional periodic overlapping mesh systems.

I. Introduction

Unstructured mesh approaches have become well established for steady-state flow simulations due to the flexibility they afford for dealing with complex geometries. For unsteady flows with moving boundaries, such as aeroelastic problems, implicit time-integration strategies are required for the efficient solution of the flow equations. For problems with strong periodic content, such as turbomachinery flows or rotorcraft aerodynamics, implicit time-spectral methods can be used to substantially reduce the cost of computing the full time-dependent solution for a given level of accuracy.

The time spectral method is based on the use of discrete Fourier analysis. The harmonic balance method, which has been developed by Hall[7] and McMullen,[15,16] transforms the unsteady equations in the physical domain to a set of steady equations in the frequency domain. Subsequently, Gopinath[5,20] proposed to solve the time spectral equations directly in the time domain. The time spectral method was shown to be faster than the dual-time stepping implicit methods using backwards difference time formulae for time periodic computations, such as turbomachinery flows,[15,20] oscillatory pitching airfoil/wing cases,[5,11] flapping wing,[17] helicopter rotor[3,4] and vortex shedding problems.[16]

In practice, the time spectral method can only be applied to periodic flows. However, there are many quasi-periodic flows that combine strong periodic content with a slow mean flow transient, such as an oscillating pitching and climbing airfoil or wing, and a maneuvering helicopter rotor. In such cases, practical time-stepping simulations can become very costly since the time step is limited by the accuracy considerations imposed by the fast periodic flow features (i.e. time steps typically smaller than 1 degree of rotation for rotorcraft configurations) while long time histories must be simulated to capture the slower transient effects.

In previous work, we have introduced a hybrid BDF/time-spectral approach which aims to simulate quasi-periodic flows with slow transients combined with relatively fast periodic content using global BDF

*Professor, AIAA Associate Fellow; email: mavriplis@uwyo.edu
†Research Scientist, AIAA member; email: zyang@uwyo.edu
‡Graduate Research Assistant, AIAA member; email:nmundis@uwyo.edu

time step sizes of the order of the period length, while making use of the properties of the time-spectral approach to capture accurate details of the periodic flow components.[21,22] The idea is rooted in the concept of polynomial subtraction for spectral methods, discussed by Gottlieb and Orzag[6] and originally credited to Lanczos.[10] In this approach, the non-periodic (transient) portion of a quasi-periodic function is subtracted from the function and represented with a polynomial basis set. The remaining function is periodic and thus can be approximated efficiently with spectral basis functions.

Overlapping mesh systems constitute one of the most common approaches for simulating complex configurations with relative motion such as rotor-fuselage interactions or wind-turbine rotor-tower configurations. Thus, the extension of time spectral methods to dynamically overlapping mesh systems represents an important capability that is required if these methods are to be used for practical rotorcraft or wind turbine engineering simulation problems. The extension of time-spectral methods to overlapping mesh systems represents a non-trivial problem. The efficiency of the time-spectral temporal discretization is predicated on the existence of a smooth, continuous and periodic time history at each grid point or cell, that can be approximated efficiently using harmonic basis functions. However, for overlapping mesh systems, individual grid cells near overlap fringe regions may toggle back and forth between active, fringe, and "blanked out" values as the mesh overlap configuration varies in time, leading to discontinuous time histories at individual cells. In order to apply time-spectral methods in such cases, a continuous smooth time history must be reconstructed at all grid cells.

The various time instances or harmonic solutions in the time spectral approach are coupled and must be solved simultaneously. However, the coupling only comes in through a source term and each individual time instance may be solved in parallel with the other time instances. This introduces an additional dimension for achieving parallelism compared to time-domain computations, where progress in the time dimension is necessarily sequential. In our implementation, two levels of parallelism are introduced, the first in the spatial dimension, and the second in the time dimension where the various time instances are solved by spawning multiple instances of the spatial solver on a parallel computer. The implementation is performed with minimal modifications to an existing steady-state unstructured multigrid solver, and using multiple MPI communicators to manage communication for the coupling between the harmonic solution instances, and within each time instance solution in the spatial dimension.

In the following sections, we first outline the governing equations and the base flow solver. We then discuss the time spectral method and subsequently the hybrid BDF/time-spectral approach. The parallel implementation of the method is also described taking into consideration optimization on multi-core architectures and through a strategy that requires minimal modifications to existing CFD solvers, as described in subsection II D. The BDF/time-spectral method is then demonstrated on two three-dimensional problems of practical interest. Next, we describe the extension of the time spectral approach to overlapping mesh systems and demonstrate this approach for a two-dimensional pitching-plunging airfoil case. Finally, prospects for further improvements are discussed in the conclusions section.

II. Governing Equations

A. Base Solver

The Navier-Stokes equations in conservative form can be written as:

$$\frac{\partial \mathbf{U}}{\partial t} + \nabla \cdot (\mathbf{F}(\mathbf{U}) + \mathbf{G}(\mathbf{U})) = 0 \tag{1}$$

where $\mathbf{U}$ represents the vector of conserved quantities (mass, momentum, and energy), $\mathbf{F}(\mathbf{U})$ represents the convective fluxes and $\mathbf{G}(\mathbf{U})$ represents the viscous fluxes. Integrating over a (moving) control volume $\Omega(t)$, we obtain:

$$\int_{\Omega(t)} \frac{\partial \mathbf{U}}{\partial t} dV + \int_{\partial\Omega(t)} (\mathbf{F}(\mathbf{U}) \cdot \vec{\mathbf{n}}) dS + \int_{\partial\Omega(t)} (\mathbf{G}(\mathbf{U}) \cdot \vec{\mathbf{n}}) dS = 0 \tag{2}$$

Using the differential identity

$$\frac{\partial}{\partial t} \int_{\Omega(t)} \mathbf{U} dV = \int_{\Omega(t)} \frac{\partial \mathbf{U}}{\partial t} dV + \int_{\partial\Omega(t)} \mathbf{U}(\dot{\mathbf{x}} \cdot \vec{\mathbf{n}}) dS \tag{3}$$

where $\dot{\mathbf{x}}$ and $\vec{\mathbf{n}}$ are the velocity and normal of the interface $\partial\Omega(t)$, respectively, equation (2) becomes:

$$\frac{\partial}{\partial t}\int_{\Omega(t)} \mathbf{U}dV + \int_{\partial\Omega(t)} (\mathbf{F}(\mathbf{U}) - \mathbf{U}\dot{\mathbf{x}}) \cdot \vec{\mathbf{n}}dS + \int_{\partial\Omega(t)} \mathbf{G}(\mathbf{U}) \cdot \vec{\mathbf{n}}dS = 0 \tag{4}$$

Considering $\mathbf{U}$ as cell averaged quantities, these equations are discretized in space as:

$$\frac{\partial}{\partial t}(V\mathbf{U}) + \mathbf{R}(\mathbf{U}, \dot{\mathbf{x}}(\mathbf{t}), \vec{\mathbf{n}}(\mathbf{t})) + \mathbf{S}(\mathbf{U}, \vec{\mathbf{n}}(\mathbf{t})) = \mathbf{0} \tag{5}$$

where $\mathbf{R}(\mathbf{U}, \dot{\mathbf{x}}, \vec{\mathbf{n}}) = \int_{\partial\Omega(t)} (\mathbf{F}(\mathbf{U}) - \dot{\mathbf{x}}\mathbf{U}) \cdot \vec{\mathbf{n}}dS$ represents the discrete convective fluxes in ALE form, $S(\mathbf{U}, \vec{\mathbf{n}})$ represents the discrete viscous fluxes, and V denotes the control volume. In the discrete form, $\dot{\mathbf{x}}(\mathbf{t})$ and $\vec{\mathbf{n}}(\mathbf{t})$ now represent the time varying velocities and surface normals of the control-volume boundary faces.

The Navier-Stokes equations are discretized by a central difference finite-volume scheme with additional matrix-based artificial dissipation on hybrid meshes which may include tetrahedra, pyramids, prisms and hexahedra in three dimensions. Second-order accuracy is achieved using a two-pass construction of the artificial dissipation operator, which corresponds to an undivided biharmonic operator. A single unifying edge-based data-structure is used in the flow solver for all types of elements. For the base solver, the time derivative in equation (5) is discretized using a second order backwards difference (BDF2) scheme, resulting in a non-linear system to be solved at each time step. The implicit solution is achieved using a line-implicit agglomeration multigrid algorithm where a first-order accurate discretization is employed for the convective terms on coarse grid levels.[12,13]

B. Time Spectral Method

If the flow is periodic in time, the variables $\mathbf{U}$ can be represented by a discrete Fourier series. The discrete Fourier transform of $\mathbf{U}$ in a period of T is given by[5]

$$\widehat{\mathbf{U}}_k = \frac{1}{N}\sum_{n=0}^{N-1} \mathbf{U}^n e^{-ik\frac{2\pi}{T}n\Delta t} \tag{6}$$

where N is the number of time intervals and $\Delta t = T/N$. The Fourier inverse transform is then given as

$$\mathbf{U}^n = \sum_{k=-\frac{N}{2}}^{\frac{N}{2}-1} \widehat{\mathbf{U}}_k e^{ik\frac{2\pi}{T}n\Delta t} \tag{7}$$

Note that this corresponds to a collocation approximation, i.e. the function $\mathbf{U}(t)$ is projected into the space spanned by the truncated set of complex exponential (spectral) functions, and the expansion coefficients (in this case the $\widehat{\mathbf{U}}_k$) are determined by requiring $\mathbf{U}(t)$ to be equal to its projection at N discrete locations in time, as given by equations (6) and (7).
Differentiating equation (7) in time, we obtain:

$$\frac{\partial}{\partial t}(\mathbf{U}^n) = \frac{2\pi}{T}\sum_{k=-\frac{N}{2}}^{\frac{N}{2}-1} ik\widehat{\mathbf{U}}_k e^{ik\frac{2\pi}{T}n\Delta t} \tag{8}$$

Substituting equation (6) into equation (8), we get[2,8]

$$\frac{\partial}{\partial t}(\mathbf{U}^n) = \sum_{j=0}^{N-1} d_n^j \mathbf{U}^j \tag{9}$$

where

$$d_n^j = \begin{cases} \frac{2\pi}{T}\frac{1}{2}(-1)^{n-j}cot(\frac{\pi(n-j)}{N}) & n \neq j \\ 0 & n = j \end{cases}$$

for an even number of time instances and

$$d_n^j = \begin{cases} \frac{2\pi}{T}\frac{1}{2}(-1)^{n-j} cosec(\frac{\pi(n-j)}{N}) & n \neq j \\ 0 & n = j \end{cases}$$

for an odd number of time instances. The collocation approach for solving equation (5) consists of substituting the collocation approximation for the continuous function $\mathbf{U}(t)$ given by equation (7) into equation (5), and requiring equation (5) to hold exactly at the same N discrete locations in time (i.e. multiplying (5) by the dirac delta test function $\delta(t - t^n)$ and integrating over all time), yielding:

$$\sum_{j=0}^{N-1} d_n^j V^j \mathbf{U}^j + \mathbf{R}(\mathbf{U^n}, \dot{\mathbf{x}}^\mathbf{n}, \vec{\mathbf{n}}^\mathbf{n}) + \mathbf{S}(\mathbf{U^n}, \vec{\mathbf{n}}^\mathbf{n}) = 0 \qquad n = 0, 1, 2, ..., N-1 \tag{10}$$

This results in a system of N equations for the N time instances $\mathbf{U}^n$ which are all coupled through the summation over the time instances in the time derivative term. The spatial discretization operators remain unchanged in the time-spectral approach, with only the requirement that they be evaluated at the appropriate location in time. Thus, the time-spectral method may be implemented without any modifications to an existing spatial discretization, requiring only the addition of the temporal discretization coupling term, although the multiple time instances must be solved simultaneously due to this coupling.

C. Hybrid BDF/Time Spectral Method

The idea of polynomial subtraction for quasi-periodic functions is to subtract out the non-periodic transient, which can be modeled using a polynomial basis set, and to approximate the remaining purely periodic component with a spectral basis set.[6] From the point of view of a collocation method, this corresponds to using a mixed spectral/polynomial basis set for the projection of the continuous solution (in the time dimension).

We proceed by splitting the quasi-periodic temporal variation of the solution into a periodic and slowly varying mean flow as:

$$\mathbf{U}(t) = \sum_{k=-\frac{N}{2}}^{\frac{N}{2}-1} \widehat{\mathbf{U}}_k e^{ik\frac{2\pi}{T}n\Delta t} + \bar{\mathbf{U}}(t) \tag{11}$$

where the slowly varying mean flow is approximated by a collocation method using a polynomial basis set as:

$$\bar{\mathbf{U}}(t) = \phi_{12}(t)\mathbf{U}^{m+1} + \phi_{11}(t)\mathbf{U}^m \tag{12}$$

for a linear variation and

$$\bar{\mathbf{U}}(t) = \phi_{23}(t)\mathbf{U}^{m+1} + \phi_{22}(t)\mathbf{U}^m + \phi_{21}(t)\mathbf{U}^{m-1} \tag{13}$$

for a quadratic variation in time. Here $\mathbf{U}^m$ and $\mathbf{U}^{m+1}$ represent discrete solution instances in time usually taken as the beginning and ending points of the considered period in the quasi-periodic motion (and $\mathbf{U}^{m-1}$ corresponds to the beginning point of the previous period). In the first case, $\phi_{12}(t)$ and $\phi_{11}(t)$ correspond to the linear interpolation functions given by:

$$\phi_{11}(t) = \frac{t^{m+1} - t}{T} \tag{14}$$

$$\phi_{12}(t) = \frac{t - t^m}{T} \tag{15}$$

with the period given as $T = t^{m+1} - t^m$. Similarly, the $\phi_{23}(t), \phi_{22}(t), \phi_{21}(t)$ are given by the corresponding quadratic interpolation functions. Note that in this case, the collocation approximation leads to the determination of the Fourier coefficients as:

$$\widehat{\mathbf{U}}_k = \frac{1}{N}\sum_{n=0}^{N-1} \tilde{\mathbf{U}}^n e^{-ik\frac{2\pi}{T}n\Delta t} \tag{16}$$

with $\tilde{\mathbf{U}}^n = \mathbf{U}^n - \bar{\mathbf{U}}^n$ defined as the remaining periodic component of the function after polynomial subtraction. Differentiating equation (11) and making use of equations (9) and (16) we obtain the following expression for the time derivative:

$$\frac{\partial}{\partial t}(\mathbf{U}^n) = \sum_{j=0}^{N-1} d_n^j \tilde{\mathbf{U}}^j + \phi'_{12}(t_n)\mathbf{U}^{m+1} + \phi'_{11}(t_n)\mathbf{U}^m \tag{17}$$

for the case of a linear polynomial functions in time. The $\phi'_{12}(t_n)$ and $\phi'_{11}(t_n)$ represent the time derivatives of the polynomial basis functions (resulting in the constant values $\frac{-1}{T}$ and $\frac{1}{T}$ in this case), and the various time instances are given by:

$$t_j = t_m + \frac{j}{N}(t_{m+1} - t_m), \qquad j = 0, \ldots, N-1$$

We also note that $\bar{\mathbf{U}}(t_m) = \mathbf{U}^m = \mathbf{U}(t_m)$ and thus we have $\tilde{\mathbf{U}}^0 = 0$. In other words, the constant mode in the spectral representation must be taken as zero, since it is contained in the polynomial component of the function representation. Therefore, the $j = 0$ component in the summation can be dropped, and rewriting equation (17) in terms of the original time instances $\mathbf{U}^n$ we obtain:

$$\frac{\partial}{\partial t}(\mathbf{U}^n) = \sum_{j=1}^{N-1} d_n^j \mathbf{U}^j - (\sum_{j=1}^{N-1} d_n^j \phi_{12}(t_j) - \phi'_{12}(t_n))\mathbf{U}^{m+1} - (\sum_{j=1}^{N-1} d_n^j \phi_{11}(t_j) - \phi'_{11}(t_n))\mathbf{U}^m \tag{18}$$

Finally, the above expression for the time derivative is substituted into equation (5) which is then required to hold exactly at time instances $j = 1, 2, ..., N-1$ and $j = N$ (which corresponds to the $m+1$ time instance):

$$\sum_{j=1}^{N-1} d_n^j V^j \mathbf{U}^j - (\sum_{j=1}^{N-1} d_n^j \phi_{12}(t_j) - \phi'_{12}(t_n))V^{m+1}\mathbf{U}^{m+1} - (\sum_{j=1}^{N-1} d_n^j \phi_{11}(t_j) - \phi'_{11}(t_n))V^m\mathbf{U}^m \tag{19}$$
$$+\mathbf{R}(\mathbf{U^n}, \dot{\mathbf{x}}^\mathbf{n}, \vec{\mathbf{n}}^\mathbf{n}) + \mathbf{S}(\mathbf{U^n}, \vec{\mathbf{n}}^\mathbf{n}) = 0 \qquad n = 1, 2, ..., N$$

As previously, we have N coupled equations with N unknown time instances, although in this case the $j = 0$ time instance which corresponds to the $\mathbf{U}^m$ values are known from the solution of the previous period, while the $j = N$ or $\mathbf{U}^{m+1}$ values are not known, since these are not equal to the $j = 0$ values as they would be in a purely periodic flow. In the case of vanishing periodic content, summation terms involving the d_n^j coefficients vanish by virtue of equation (17) with $\tilde{\mathbf{U}}^j = 0$ and it is easily verified that the above formulation reduces to a first-order backwards difference scheme with a time step equal to the period T. On the other hand, for purely periodic motion, we have $\mathbf{U}^{m+1} = \mathbf{U}^m$ which results in cancellation of the polynomial derivative terms $\phi'_{12}(t_n)$ and $\phi'_{11}(t_n)$. Furthermore, using the identities $\phi_{12}(t_j) + \phi_{11}(t_j) = 1$, and $\sum_{j=0}^{N-1} d_n^j = 0$, it can be seen that the remaining polynomial terms reduce to the missing $j = 0$ instance in the summation. Given the equality $\mathbf{U}^{m+1} = \mathbf{U}^m$, the last equation at $j = N$ becomes identical to the $j = 0$ equation and the time-spectral method given by equation (10) is recovered.

In this description we have used linear polynomials corresponding to a BDF1 time-stepping scheme for clarity. In practice, BDF2 time-stepping schemes are required for accuracy purposes, and the equivalent scheme based on quadratic polynomials is given as:

$$\sum_{j=1}^{N-1} d_n^j V^j \mathbf{U}^j - (\sum_{j=1}^{N-1} d_n^j \phi_{23}(t_j) - \phi'_{23}(t_n))V^{m+1}\mathbf{U}^{m+1} \tag{20}$$
$$-(\sum_{j=1}^{N-1} d_n^j \phi_{22}(t_j) - \phi'_{22}(t_n))V^m\mathbf{U}^m - (\sum_{j=1}^{N-1} d_n^j \phi_{21}(t_j) - \phi'_{21}(t_n))V^{m-1}\mathbf{U}^{m-1}$$
$$+\mathbf{R}(\mathbf{U^n}, \dot{\mathbf{x}}^\mathbf{n}, \vec{\mathbf{n}}^\mathbf{n}) + \mathbf{S}(\mathbf{U^n}, \vec{\mathbf{n}}^\mathbf{n}) = 0 \qquad n = 1, 2, ..., N$$

where the values $\mathbf{U}^{m-1}$ and $\mathbf{U}^m$, which correspond to the time instances at the beginning and end of the previous period are known from the solution of earlier periods, and $\mathbf{U}^{m+1} = \mathbf{U}^N$ as previously.

D. Parallel Implementation

A principal advantage of the TS and BDFTS approaches is that they can be implemented with relative ease into existing steady-state codes because the spatial discretization operator is unchanged from the baseline code. However, both approaches result in multiple time instances which are coupled and must be solved simultaneously. On the one hand, this provides the opportunity for exploiting parallelism in the time direction, as compared to traditional time-stepping schemes which necessarily advance sequentially in time. This feature may prove to be particularly enabling with the advent of rapidly expanding hardware parallelism, particularly for cases where parallelism in the spatial dimension has been exhausted (perhaps due to the adequacy of moderate grid sizes). A non-intrusive approach for implementing TS/BDFTS methods in parallel can be achieved by introducing separate MPI communicators. The baseline solver operates in parallel and makes use of an MPI communicator to exchange information between neighboring spatial grid partitions. Our strategy consists of replicating instances of the entire solver on additional processors for each required time instance in the TS/BDFTS formulation. In this manner, the code remains unchanged apart from the addition of a source term which provides the coupling between time instances due to the TS time derivative term. This fully parallel implementation contains two types of inter-processor communication: communication between spatial partitions within a single time instance, and communication between all of the time instances. A simple approach is to use a separate additional MPI communicator for the latter type of communication, leaving all original spatial communication routines unchanged. One of the drawbacks of the TS/BDFTS methods is that each time instance must broadcast its entire solution field to all other time instances, which can result in a significant amount of communication. Various strategies for communicating the different time instances to all processors have been investigated. Currently, a Round-Robin approach is implemented, where each processor sends its time instance to a single neighboring processor. The received time instance is added to the time derivative source term on the local processor, and then passed on to the next processor. By repeating this procedure N times, where N is the number or time instances, the complete time derivative involving summations from all time instances is accumulated without the requirement of creating any local temporary copies of the additional time instances or performing any communication intensive broadcast operations. For multicore and/or multiprocessor hardware nodes within a distributed memory parallel machine, the optimal strategy consists of placing all time instances of a particular spatial partition on the same node, with each time instance being assigned to a local core, while the individual spatial partitions are distributed across the nodes of the machine. In this manner, all time-instance communication generated by the TS/BDFTS methods (which is spatially local) becomes node local and benefits from the shared memory and/or faster local communication bandwidth within a node.

III. Quasi-Time Spectral Results

In previous work, the time-spectral and BDF-time-spectral methods have been validated on simple periodic and quasi-periodic problems in two and three dimensions for simple airfoil and wing configurations. The performance of the BDFTS approach is detailed for two three-dimensional test cases in the following subsections illustrating the strengths and challenges of this method.

A. Pitching climbing wing

The first test case consists of a three-dimensional inviscid pitching-climbing AGARD 445.6 wing. An unstructured mesh of 40460 nodes and 224531 tetrahedra is used for this calculation and is shown in Figure 1a. The freestream Mach number is set to 0.511 and the wing undergoes a forced pitching motion, while at the same time undergoing a slow change in mean angle of attack and a transient rising motion. The time dependent angle of attack and the prescribed airfoil forward and upward velocities are shown in Figure 1b. The mesh is displaced as a solid body in this case, pitching and translating as defined by the wing motion. The time dependent flow field is computed firstly using a second-order accurate backward difference (BDF2) time implicit scheme using a 64 time steps per period. The same flow field is also computed using the BDF time-spectral approach using $N = 5, 7, 9$ time instances per period. The complete simulation includes 12 periods of pitching motion after which the transient vanishes as seen in Figure 1b.

Figure 2a shows the comparison of the computed drag coefficient. Although both lift and drag coefficient histories are available for comparison, the drag coefficient time history contains more than one important harmonic frequency as can be surmised from the plot. In this case, the BDFTS scheme with $N = 5, 7, 9$

time instance shows very good agreement with the reference BDF2 solution computed using 64 time steps per period. Figure 2b shows additional detail for the comparison of the computed drag coefficients, where it can be seen that the BDFTS results converge uniformly to the BDF2 reference solution as the number of time instances is increased. This relatively simple case represents a near ideal scenario for the BDFTS scheme since the time histories are very smooth with relatively low spectral content and thus can be captured accurately with small numbers of time instances per period.

B. UH-60A Transient Pull-Up Maneuver Test Case

A more realistic and challenging case can be found in the simulation of the Utility Tactical Transport Aerial System (UTTAS) pull-up maneuver of the UH-60A helicopter. Detailed measurements of blade aerodynamics and structural dynamics load measurements have been conducted on this configuration as part of the NASA-Army UH-60A Airloads Program which investigated a wide range of flight conditions. An extensive documentation of the flight test program can be found in Bousman and Kufeld .[1,9] The operating envelope of the helicopter plotted as variation of vehicle weight coefficient with advance ratio is shown in Figure 3. The limiting factors for these flight conditions are the maximum thrust limit because of retreating blade stall and maximum sectional airfoil lift that can be generated. McHugh et al.[14] determined the maximum thrust boundary using wind-tunnel tests which is represented in the figure. Note that all the steady flight conditions lie below the McHugh boundary. Figure 3 also shows the variation of weight coefficient with advance ratio for the UTTAS pull-up maneuver. The maneuver begins quite close to the maximum level flight speed of the aircraft and achieves a peak load factor of 2.1g, which exceeds the steady state McHugh boundary. Therefore the UTTAS pull-up maneuver is a challenging flight condition in terms of predictive capability.

The specific computational case consists of a transition from the initial periodic high speed forward flight condition to a steady climb condition in about 40 revolutions of the rotor (approximately 10 seconds). In this case, the UH-60A aircraft is modeled as an isolated flexible rotor. In order to further simplify the problem, we make use of prescribed flight path and prescribed aeroelastic rotor deflections obtained from a fully coupled CFD-CSD simulation performed previously in reference.[19] Figure 4(a) shows the prescribed speed and pitch angle of the hub. Figure 4(b) shows the prescribed displacement and the Wiener-Milenkovic parameters(c1, c2 and c3) used to define the aeroelastic motion of the blade tip. The prescribed motion is applied in four different operations to the computational mesh. Firstly, the rotational motion is applied by directly rotating the mesh by the required angle about the hub axis. Next, the mesh is pitched as a solid body and translated according to the prescribed hub motion and attitude. Finally, the aeroelastic deflections are applied to the surface grid for each blade, and the interior mesh is then deformed in response to the surface deflections using a spring analogy mesh deformation approach. These operations are performed at each time step in the time-domain (BDF2) simulation, and for each time instance in the time spectral or BDF/time-spectral approach.

The transient test case was simulated using the BDF/time-spectral approach with N=7,9, and 11 time instances. A baseline BDF2 time-domain simulation with a 0.5 degree time step was also performed for comparison purposes. Figures 6(a), 6(b) and 6(c) show the comparison of the predicted forces in x, y and z directions on one blade between BDF and BDFTS with different time instances. The forces are plotted as functions of time in units of revolution. The forces predicted by BDFTS show generally good agreement with the results obtained using BDF. Figure 6(d) shows the comparison of the predicted rotor thrust between BDF, BDFTS and the flight test measurements. The measured data is averaged over each revolution and therefore appears smoother. The pattern and averaged amplitude of the lift predicted by BDF and BDFTS are in agreement with the measured data, although the BDFTS results show larger amplitude oscillations.

Figure 7 shows the comparison the pitching moment at revolution No. 6 of the transient maneuver at two spanwise stations of the rotor blade. The choice of pitching moment comparisons is intentional as these are often the most challenging aspects of rotorcraft aeromechanics to simulate accurately. The overall sectional pitching moments are reasonably predicted in this case by both BDF and BDFTS, especially at the inboard radial stations. On the outboard stations there is significant degradation in the agreement with test data in the advancing blade phase. While the discrepancies between computation and experiment can be attributed at least partially to grid resolution, the accuracy of the prescribed aeroelastic deflections, and the absence of any fuselage interaction, for the purposes of this work, the focus is on the differences between the BDFTS and time domain computational results. In this case, there is substantial variation in the BDFTS results as the number of time instances is increased, although the results appear to be approaching the BDF time histories

for the highest number of time instances. In this case, sharp variations in the pitching moment coefficient are seen at the outboard stations indicative of dynamic stall. Capturing the details of this non-smooth behavior is particularly challenging for the time spectral method and will likely require the use of greater numbers of time instances to achieve suitable accuracy. This is to be contrasted with the previous test case, where the relatively smooth time histories could be captured very accurately with as few as 5 time instances per period.

IV. Extension to Overlapping Mesh Systems

A. Formulation

As mentioned previously, the extension of time-spectral methods to overlapping mesh systems requires the availability of a continuous and smooth time history at all active mesh cells in the overlapping mesh system. In a typical overlapping mesh paradigm consisting of a near-body mesh that moves with the body and a fixed background mesh, a hole is cut out of the background mesh in the vicinity of the body where the near body mesh is active and the background mesh cells are inactive. As the body sweeps across the background mesh, the set of inactive "blanked out" background mesh cells changes in time. Thus, within a time periodic problem, there will exist background mesh cells that toggle between active and blanked out at different locations within the period. Because no flow values are computed at blanked-out cells, no time history exists at these cells during these time intervals, and a Fourier representation of the periodic time signal at these cells is no longer possible.

A simple approach for mitigating this problem is through the use of an implicit hole cutting technique.[18] In this approach, instead of deactivating flow computations in predetermined regions of the background mesh, flow values are computed at all grid cells on both grid systems. A search algorithm is then used to determine the dominant mesh in each region, based on the mesh with the smallest local resolution, and the computed flow values from the recessive mesh are overwritten with the values interpolated from the dominant mesh. In this manner, almost all mesh cells on both meshes store valid flow values at all time instances. The exceptions are cells on the background mesh that are obscured by the geometry, as illustrated in Figure 8. In order to apply a time spectral method to the complete grid system, either the set of cells intersected by the geometry must be fixed at all time instances and thus never participate in the computation, or a smooth time history must be reconstructed at cells over time intervals when they are obscured by the geometry. Clearly, in the general case, for large motions, the set of intersected cells will not be constant and reconstruction methods are required. The approach taken in this work is to formulate a Poisson equation over the set of intersected cells at a given time instance. The Poisson equation is formulated with vanishing source terms and uses Dirichlet boundary conditions given by the values in neighboring active mesh cells that surround the set of blanked out cells. The implementation of this approach is rather simple: for cells that are blanked out, rather than "blank out" the flow calculation, the flow solver is replaced with a Poisson equation solver. In this manner, all mesh cells on both meshes contain a smooth distribution of flow variables at all time instances, and the time-spectral method may be applied with no further modification. The success of this approach hinges on the ability to maintain a smooth time history for blanked-out cells as determined by the Poisson equation solution, since spectral representations rely on smoothness properties for achieving exponential error convergence.

B. Time Spectral results for overlapping mesh systems

In order to validate the proposed extension to overlapping mesh systems, two inviscid flow test cases are constructed using a NACA0012 airfoil undergoing prescribed periodic pitching and/or plunging motions in two dimensions. Overset and single standalone meshes are constructed for comparison purposes. For the overset meshes, the unstructured near-body mesh consists of 859 nodes and 1577 triangular cells and the Cartesian background mesh consists of 40,804 nodes and 40,401 square cells. Conversely, the single standalone unstructured mesh consists of 3197 nodes and 6202 triangular cells. The overlapping mesh system and standalone unstructured mesh are illustrated in Figure 9. The spacing of nodes on the airfoil surface for the near-body overset grid and the standalone grid are equivalent so as to minimize this source of disagreement in the results.

The first test case prescribes two oscillatory vertical translation modes at a Mach number of 0.50 and a mean incidence α_0 of 0.00 degrees. The translation motion is prescribed by the following equation:

$$h = h_1 sin(\omega_1 t) + h_2 sin(\omega_2 t) \tag{21}$$

where h is the total displacement height and the displacement amplitudes are taken as $h_1 = 1.0c$ and $h_2 = \frac{h_1}{4} = 0.25c$ where c denotes the airfoil chord. The reduced frequency of the first mode of translation is taken as $k_1 = 0.05$ and the reduced frequency of the second mode is taken as $k_2 = 4.0k_1 = 0.20$. The ω temporal frequencies defining the motion in equation (21) are related to the reduced frequencies as:

$$\omega = \frac{2kV_\infty}{c} \tag{22}$$

where V_∞ denotes the freestream velocity and c is the airfoil chord.

Figure 10(a) shows a comparison of the lift coefficient versus non-dimensional displacement between the time accurate method (using the second order accurate BDF2 time discretization) with 96 time steps per period and the time spectral method with N = 4, 8, and 16 time instances on the overset meshes. As can be seen in the figure, reasonable agreement between the time accurate and the time spectral method is obtained with 16 time spectral instances. Figure 10(b)shows a similar comparison using the moment coefficient instead of the lift coefficient. Again, the time spectral results using 16 time instances produce reasonable agreement with the time accurate results. A comparison between both time-spectral and time accurate results obtained on the standalone mesh and overset mesh system for this case is given in Figure 11, based on the computed lift and moment coefficient histories. The time-spectral results using N=16 instances compare well with the BDF2 time histories and the agreement between overlapping and single mesh systems is also very close. These comparisons provide evidence that the extension of the time spectral approach to overlapping mesh systems maintains the accuracy properties of the underlying time spectral method.

The second test case consists of a pitching and plunging airfoil with the motion defined as:

$$\alpha = \alpha_0 + \alpha_p sin(\omega_p t) \tag{23}$$

$$h = h_t sin(\omega_t t) \tag{24}$$

where α is the airfoil incidence, and h is the airfoil vertical position. For this case the Mach number is taken as 0.65 and the mean incidence α_0 is 1.00 deg. The pitching and plunging amplitudes are set as $\alpha_p = 2.0$ deg. and $h_t = 1.0c$ respectively. The plunging reduced frequency is prescribed as $k_t = 0.05$ and the pitching reduced frequency is taken as $k_p = 0.20$, where the relation between reduced and temporal frequencies is given by equation (21). Figure 12 compares the lift and moment coefficients, respectively, versus non-dimensional vertical displacement for the time accurate (BDF2) computations with 128 time steps per period and time spectral simulations with N = 4, 8, and 14 time instances. Reasonable agreement between time accurate and time spectral results is seen when 14 time instances are used for the time spectral method. As in the previous case, Figure 13 depicts lift and moment coefficients, respectively, for both time accurate (BDF2) and time spectral (N = 14) calculations on both overset and standalone grids. As previously, agreement between the time spectral and time accurate results is similar to the agreement obtained between the overset and standalone grids.

At this point, the reader might be curious why both test cases involve such large airfoil translations compared to more traditional pitch-only or small amplitude pitch-plunge test cases usually employed for two-dimensional airfoil problems. Such large translations are necessary to ensure that the cells of the background mesh that are initially behind the airfoil (iblank = 0) are at a later time in the dominant or non-interpolated region of the flow field (iblank = 1). If this were not the case, the differences between overset and standalone grids when solving the time spectral discretization would be trivial. As mentioned earlier, when background cells are intersected by the airfoil geometry, a Poisson equation solution is substituted for the conserved flow variables using Dirichlet boundary conditions based on the closest cells with active flow computations that are not blanked out. In this way, reasonable values of the flow variables are present in all background grid cells for all times regardless of each cell's iblank value at any given instance in time.

Figure 13 shows the time history of density as a function of time within one of the foremost cells whose iblank value is initially zero when it is intersected by the airfoil. The gray regions in each of the figures correspond to the times during which this particular cell has an iblank value of zero. As can be seen in these figures, as the number of time spectral time instances increases, the time spectral signal more closely

resembles the time accurate signal. Additionally, the time spectral signals are smooth throughout the entire period of motion, including the IBLANK = 0 regions, a property which is important for convergence of the time spectral system.

V. Future work

The BDFTS method has been shown to enable the extension of time-spectral methods to quasi-periodic flows with slow transient behavior. While the BDFTS method is capable of delivering high accuracy with relatively few time instances per period for such flows, the precise order of accuracy of this temporal discretization remains to be investigated. For the TS approach, one would expect spectral accuracy in the presence of smooth time histories. For the BDFTS approach, the design accuracy may be expected to be highly dependent on the solution behavior. The method appears to be best suited for cases with two disparate time scales, a fast periodic motion and a slow transient motion.

An extension of the time spectral method to dynamically overlapping mesh systems has also been proposed. The approach is capable of accurately computing periodic problems for two-dimensional overlapping mesh configurations with dynamically varying mesh interpolation and iblanking patterns. Further work is required to determine the accuracy of this approach particularly at dynamically iblanked cells. Future plans involve the combination of overlapping mesh and quasi-periodic time spectral implementations and their application to realistic three dimensional rotorcraft and wind turbine problems with relative motion.

As with all time spectral methods, the achieved accuracy depends on the smoothness of the underlying solution time histories. For realistic complex problems where rapid dynamic events may occur, the use of many more time instances likely will be required for time spectral methods. Thus, future work will investigate efficient solution techniques for cases with large numbers of time instances and a detailed comparison of time spectral methods with time domain methods on an accuracy versus efficiency basis.

References

[1]G. Bousman, R. M. Kufeld, D. Balough, J. L. Cross, K. F. Studebaker, and C. D. C. D. Jennison. Flight testing the UH-60A airloads aircraft. May 1994. 50th Annual Forum of the American Helicopter Society, Washington, D. C.

[2]C. Canuto, M. Y. Hussaini, A. Quarteroni, and T. A. Zang. *Spectral Methods in Fluid Dynamics*. Springer, 1987.

[3]S. Choi and A. Datta. CFD prediction of rotor loads using time-spectral method and exact fluid-structure interface. AIAA 2008-7325, Aug. 2008.

[4]S. Choi, M. Potsdam, K. Lee, G. Iaccarino, and J. J. Alonso. Helicopter rotor design using a time-spectral and adjoint-based method. AIAA 2008-5810, Sep. 2008.

[5]A. K. Gopinath and A. Jameson. Time spectral method for periodic unsteady computations over two- and three-dimensional bodies. AIAA Paper 2005-1220, Jan. 2005.

[6]D. Gottlieb and S. A. Orszag. Numerical analysis of spectral methods: Theory and applications. CBMS-26, Regional Conference Series in Applied Mathematics, SIAM,Philadelphia, PA, 1977.

[7]K. C. Hall, J. P. Thomas, and W. S. Clark. Computation of unsteady nonlinear flows in cascades using a harmonic balance technique. *AIAA Journal*, 40(5):879–886, 2002.

[8]J. Hesthaven, S. Gottlieb, and D. Gottlieb. *Spectral Methods for Time-Dependent Problems*. Cambridge Monographs on Applied and Computational Mathematics, 2007.

[9]R. M. Kufeld. High load conditions measured on a UH-60A in maneuvering flight. *Journal of the American Helicopter Society*, 43(3):202–211, July 1998.

[10]C. Lanczos. Discourse on Fourier series. Hafner, New York, 1966.

[11]K.-H. Lee, J. J. Alonso, and E. van der Weide. Mesh adaptation criteria for unsteady periodic flows using a discrete adjoint time-spectral formulation. AIAA paper 2006-0692, Jan. 2006.

[12]D. J. Mavriplis and S. Pirzadeh. Large-scale parallel unstructured mesh computations for 3D high-lift analysis. *AIAA Journal of Aircraft*, 36(6):987–998, Dec. 1999.

[13]D. J. Mavriplis and V. Venkatakrishnan. A unified multigrid solver for the Navier-Stokes equations on mixed element meshes. *International Journal for Computational Fluid Dynamics*, 8:247–263, 1997.

[14]F. J. McHugh. What are the lift and propulsive force limits at high speeed for the conventional rotor ? May 1978. American Helicopter Society 34th Annual Forum, Washinton D.C.

[15]M. McMullen, A. Jameson, and J. J. Alonso. Acceleration of convergence to a periodic steady state in turbomachineary flows. AIAA Paper 2001-0152, Jan. 2001.

[16]M. McMullen, A. Jameson, and J. J. Alonso. Application of a non-linear frequency domain solver to the Euler and Navier-Stokes equations. AIAA Paper 2002-0120, Jan. 2002.

[17]S. Sankaran, A. Gopinath, E. V. D. Weide, C. Tomlin, and A. Jameson. Aerodynamics and flight control of flapping wing flight vehicles: A preliminary computational study. AIAA 2005-0841, Jan. 2005.

[18]J. Sitaraman, M. Floros, A. Wissink, and M. Potsdam. Parallel domain connectivity algorithm for unsteady flow computations using overlapping and adaptive grids. *Journal of Computational Physics*, 229:4703–4723, 2010.

[19]J. Sitaraman and B. Roget. Prediction of helicopter maneuver loads using a fluid-structure analysis. *Journal of Aircraft*, 46(5):1770–1784, 2009.

[20]E. van der Weide, A. K. Gopinath, and A. Jameson. Turbomachineary applications with the time spectral method. AIAA Paper 2005-4905, June 2005.

[21]Z. Yang and D. J. Mavriplis. Time spectral method for quasi-periodic unsteady computation on unstructured meshes. AIAA Paper 2010-5034, June 2010.

[22]Z. Yang, D. J. Mavriplis, and J. Sitaraman. Prediction of helicopter maneuver loads using BDF/time spectral method on unstructured meshes. AIAA Paper 2011-1122, June 2011.

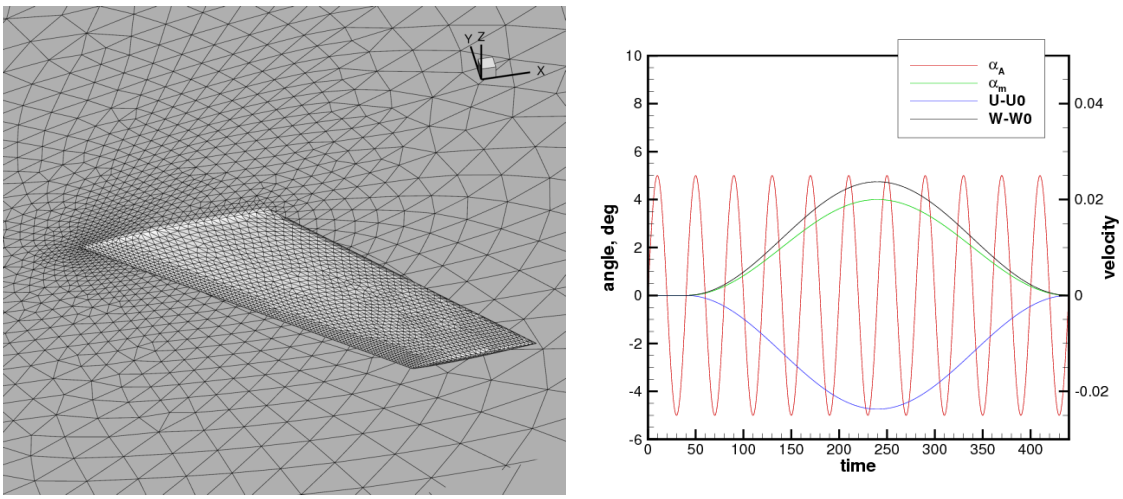

(a) (b)

Figure 1. (a) Unstructured mesh employed for three-dimensional pitching-climbing AGARD wing test case; (b) forward/upward speed and angle of attack for pitching-climbing wing test case.

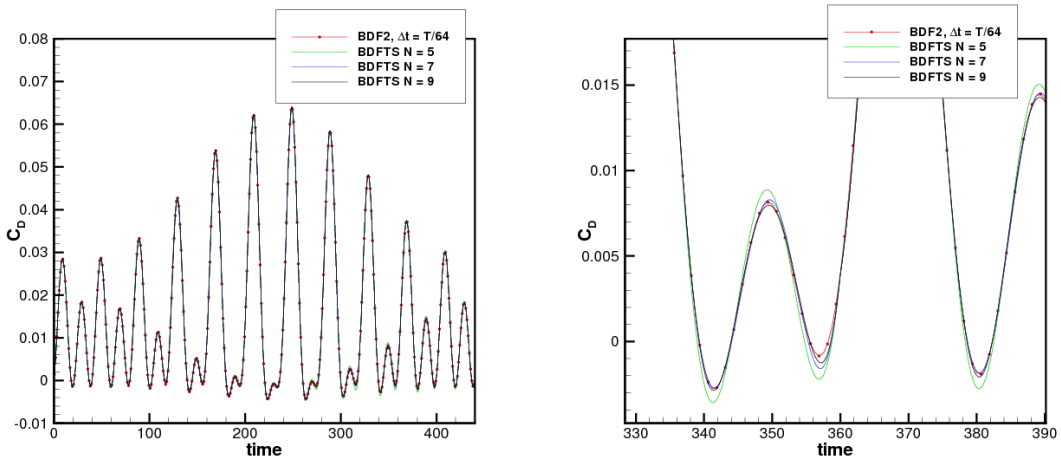

(a) (b)

Figure 2. (a) Global and (b) close up comparison of computed drag coefficient for pitching-climbing wing test case using time domain and quasi-periodic time-spectral approach.

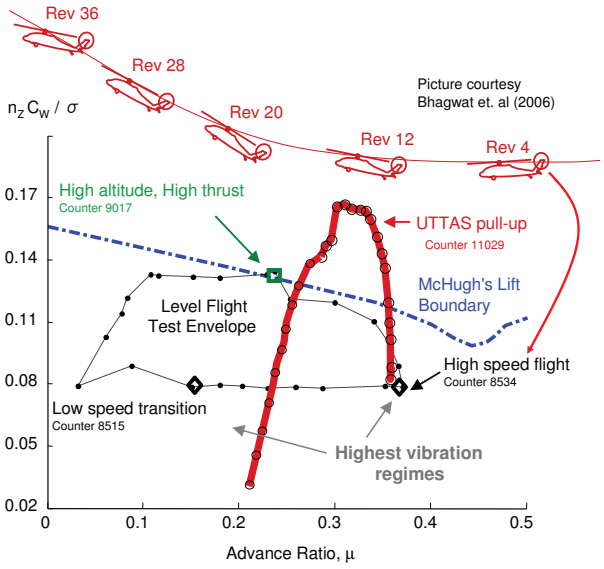

Figure 3. UH-60A flight envelope and maneuver trajectory

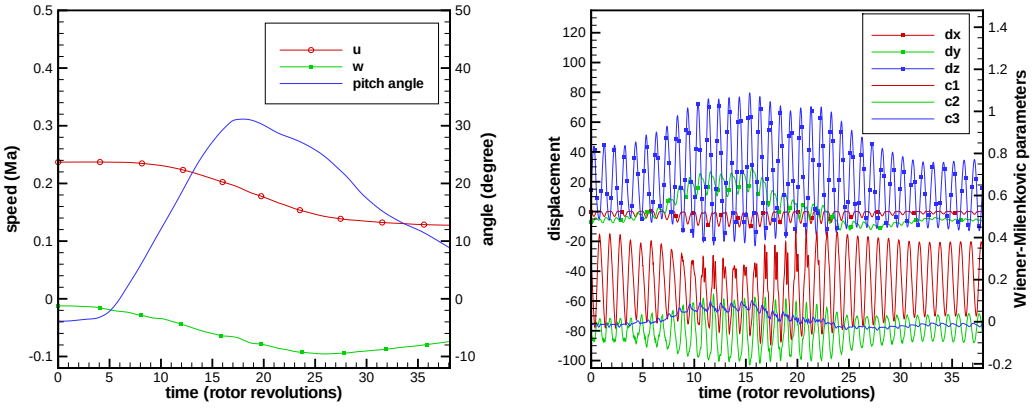

(a) Prescribed hub motion

(b) Displacement and rotation of blade tip

Figure 4. Prescribed motion used for maneuver simulation.

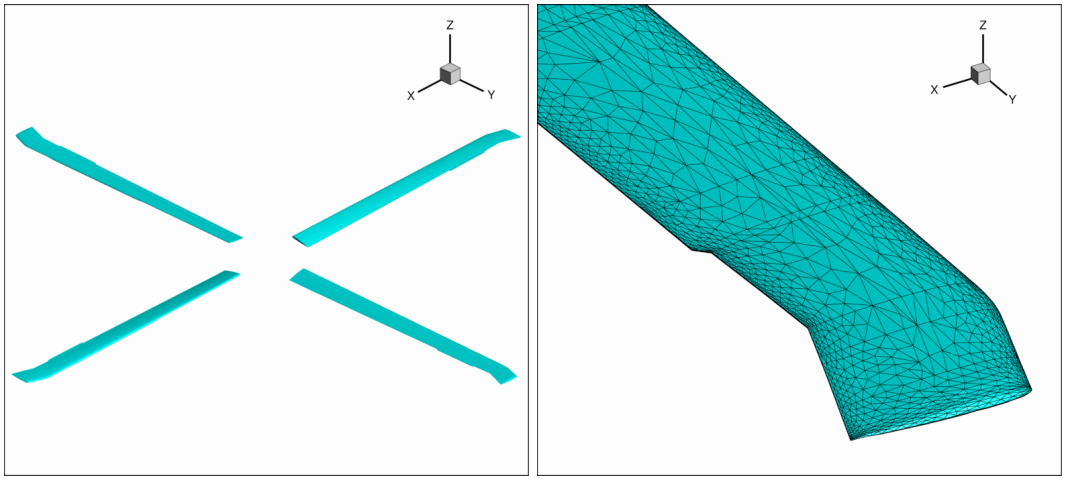

(a) Four blades (b) Mesh near blade tip

Figure 5. Unstructured mesh used for UH60A rotor configuration.

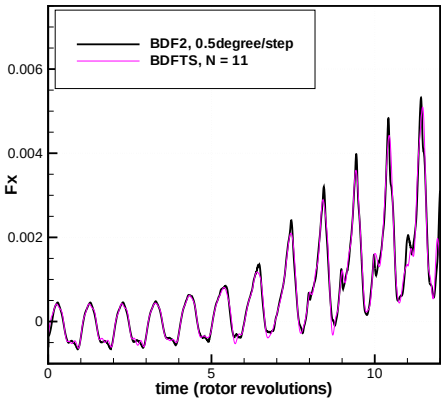

(a) force in x direction on one blade

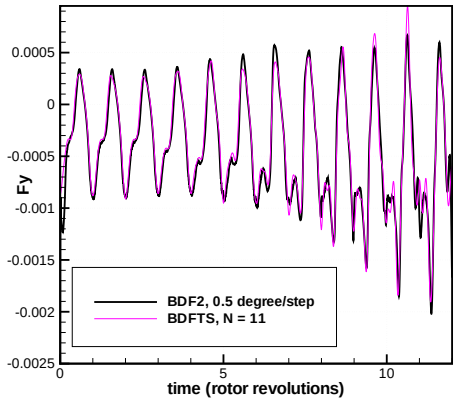

(b) force in y direction on one blade

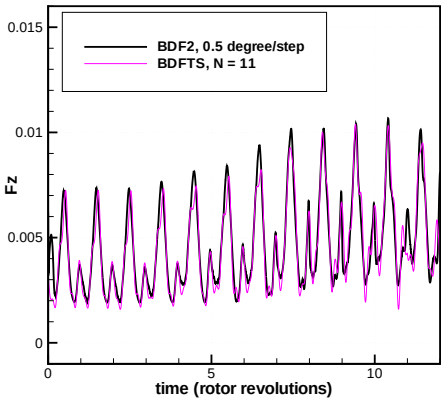

(c) force in z direction on one blade

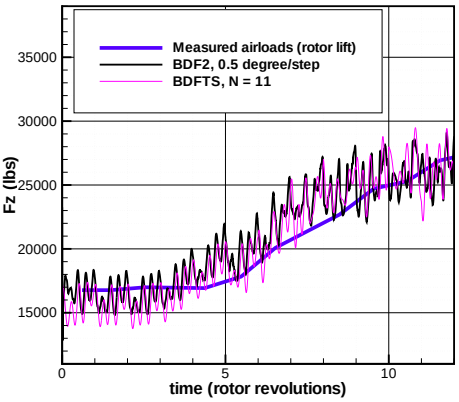

(d) total lift

Figure 6. Force comparison between time-domain BDF2 method and BDF-time-spectral method for transient UH60A pull-up maneuver including flight test data.

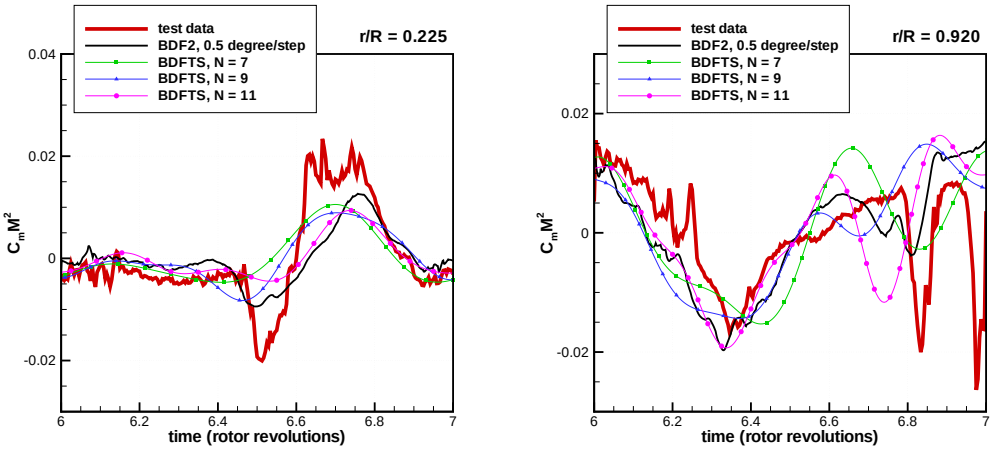

Figure 7. Nondimensional sectional pitching moment (mean removed) vs the azimuth angle at revolution 6 at (a) inboard and (b) outboard rotor stations.

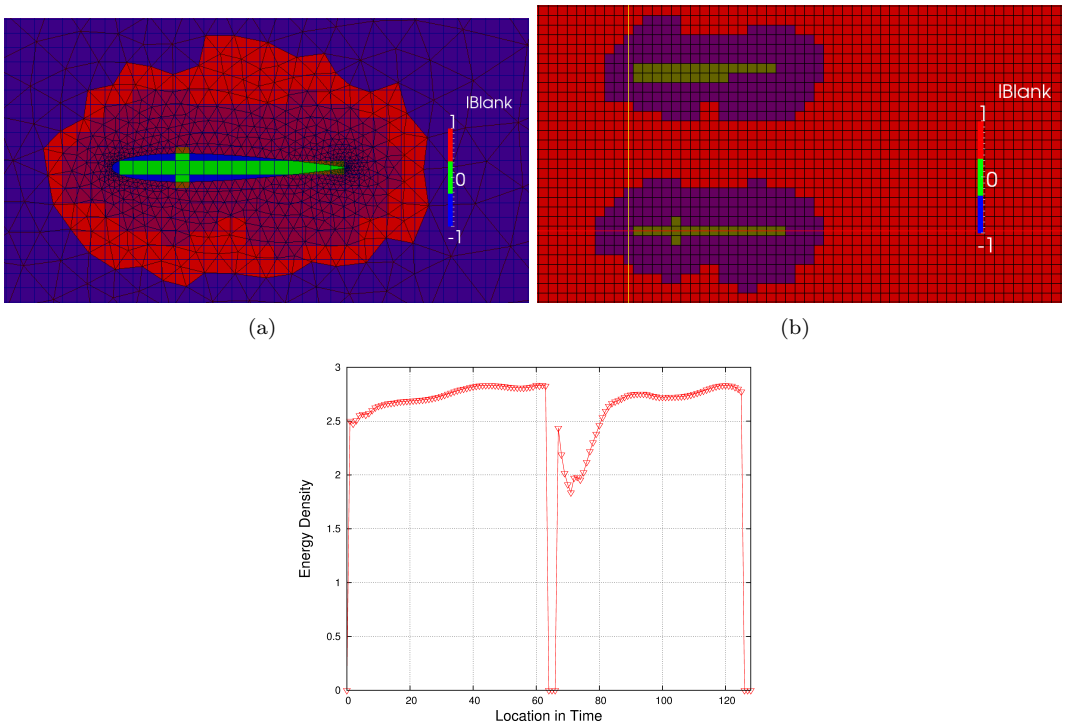

Figure 8. (a) Illustration of IBLANK values for overset mesh system in vicinity of airfoil and near-body unstructured mesh. (b) IBLANK values on background cartesian mesh for two different time instances of plunging airfoil problem. IBLANK = 1 corresponds to computed cell values; IBLANK = -1 corresponds to interpolated cell values; IBLANK = 0 corresponds to undefined cell values due to intersection with airfoil geometry. (c) Computed time history using time accurate (BDF2) scheme on overlapping mesh system at cell in background mesh that switches between IBLANK = 0 and IBLANK = +-1 during plunging airfoil computation showing discontinuous vanishing values at IBLANK=0 locations.

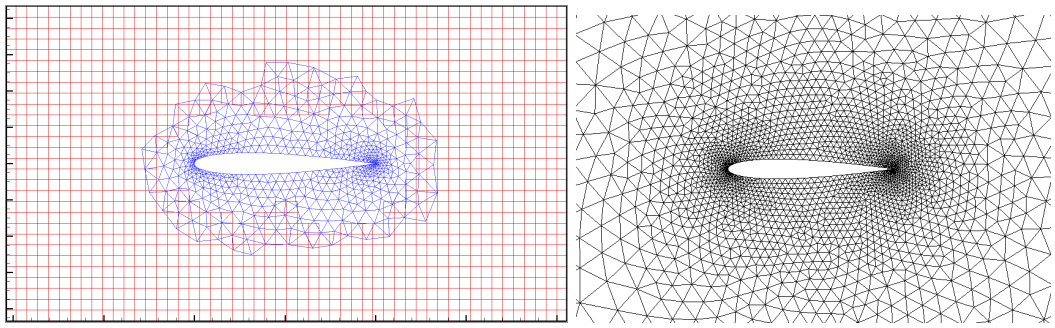

(a) (b)

Figure 9. Illustration of (a)overlapping mesh system and (b)standalone unstructured mesh used for pitching and plunging airfoil simulations

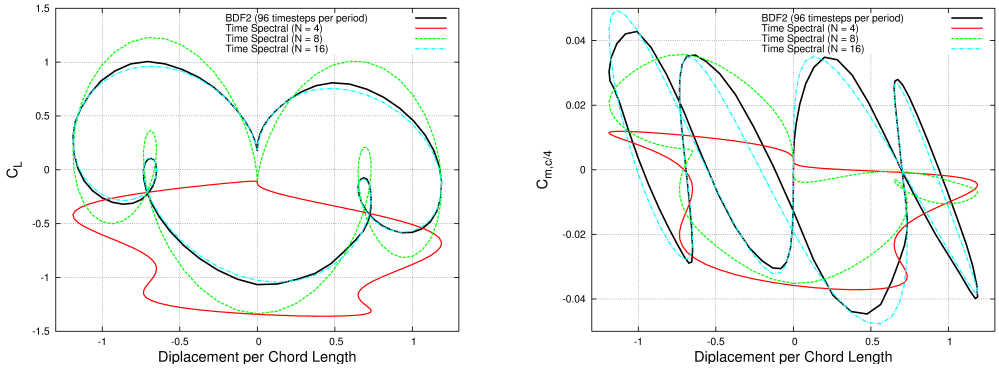

(a) (b)

Figure 10. Comparison of computed airfoil (a) lift and (b) moment coefficients for plunging airfoil problem using BDF2 time domain method and time-spectral approach with various time instances on overlapping mesh system.

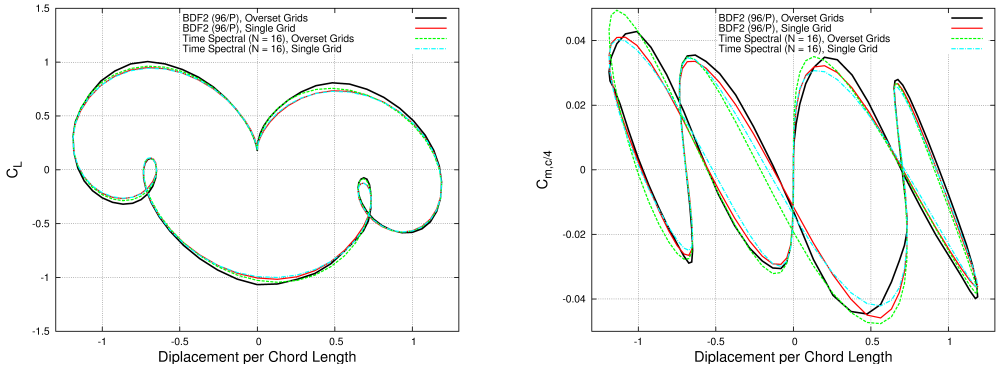

(a) (b)

Figure 11. Comparison of BDF2 and time spectral results on overlapping and single standalone mesh systems for plunging airfoil problem.

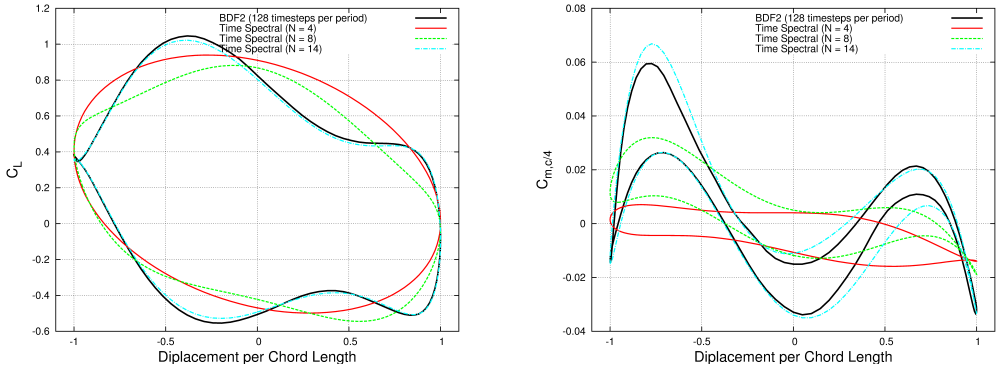

(a) (b)

Figure 12. Comparison of computed airfoil (a) lift and (b) moment coefficients for pitching and plunging airfoil problem using BDF2 time domain method and time-spectral approach with various time instances on overlapping mesh system.

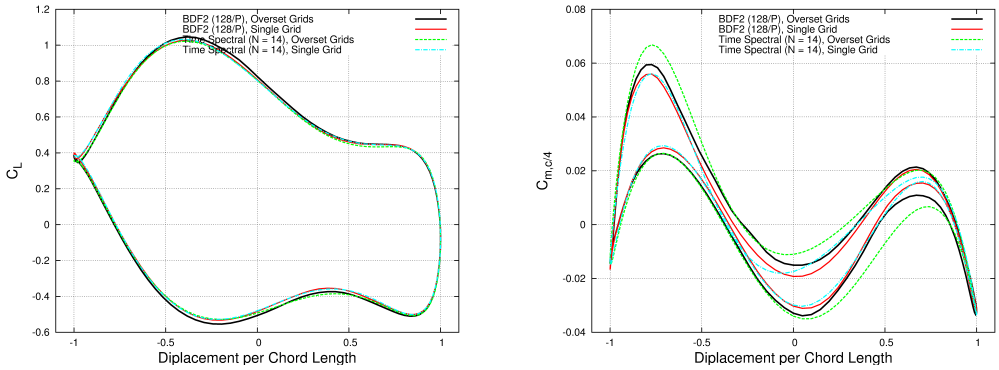

(a) (b)

Figure 13. Comparison of BDF2 and time spectral results on overlapping and single standalone mesh systems for pitching and plunging airfoil problem.

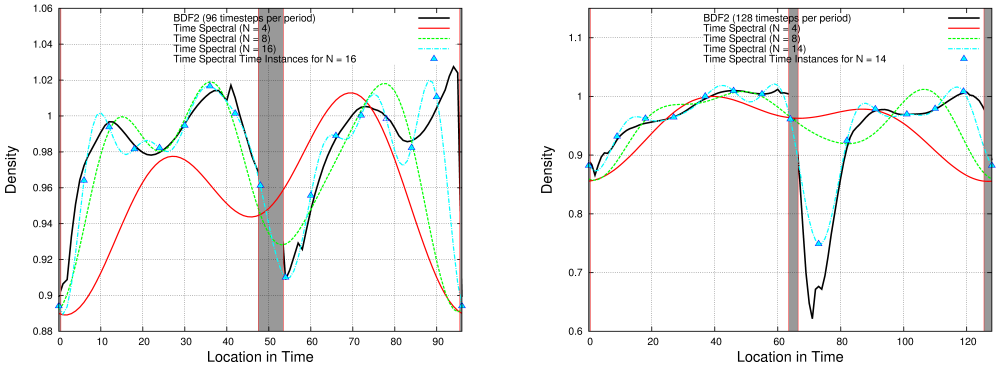

(a) (b)

Figure 14. Comparison of time histories computed using BDF2 and time spectral methods with various time instances at a particular background mesh cell for (a) plunging and (b) pitching and plunging airfoil case illustrating smooth variation of time spectral histories through IBLANK=0 regions (denoted by shaded regions)